Eastward transients in the dayside ionosphere. I. Electrodynamics on closed field lines

Magnus F. Ivarsen,[*] Jean-Pierre St-Maurice,[†] Glenn C. Hussey, and Daniel Billet
Department of Physics and Engineering Physics, University of Saskatchewan, Saskatoon, Saskatchewan, Canada

Devin R. Huyghebaert[‡]
Leibniz Institute of Atmospheric Physics, Kühlungsborn, Germany

Yaqi Jin
Department of Physics, University of Oslo, Oslo, Norway

Yukinaga Miyashita[§]
Space Science Division, Korea Astronomy and Space Science Institute, Daejeon, South Korea

Satoshi Kasahara
Department of Earth and Planetary Science, University of Tokyo, Bunkyō, Tokyo, Japan

Kaili Song and P. T. Jayachandran
Physics Department, University of New Brunswick, Fredericton, New Brunswick, Canada

Shoichiro Yokota
Department of Earth and Space Science, Osaka University, Toyonaka, Osaka, Japan

Yoshizumi Miyoshi, Kazuhiro Yamamoto, and Atsuki Shinbori
Institute for Space-Earth Environmental Research, Nagoya University, Nagoya, Aichi, Japan

Yoshiya Kasahara
Graduate School of Natural Science and Technology, Kanazawa University, Kanazawa, Ishikawa, Japan

Iku Shinohara
Institute of Space and Astronautical Science, Japan Aerospace Exploration Agency, Sagamihara, Kanagawa, Japan

Ayako Matsuoka
Data Analysis Center for Geomagnetism and Space Magnetism, Kyoto University, Kyoto, Kyoto, Japan

(Received 8 January 2025; accepted 19 August 2025; published 8 October 2025)

At night in Earth's polar regions, energetic aurorae frequently penetrate into the atmosphere, with the peculiar effect of driving turbulent electrojet currents in the bottomside ionosphere. During the day, however, Earth's plasma environment becomes highly conductive, owing to the constant flux of extreme ultraviolet radiation emitted from the Sun. The high-conductivity plasma in the dayside ionosphere can effectively short out plasma turbulence around aurorae, and so electrojet turbulence is thought rare in the dayside high-latitude ionosphere. In this paper we show observations to the contrary. During the onset of the 23 April 2023 geomagnetic storm, we observed prolific small-scale plasma turbulence in the dayside *E* region on closed magnetic field lines just equatorward of the cusp. Using data from two orbiting satellites, we infer the locations of the cusp and the distributed presence of diffuse aurorae, through observations of electron fluxes and wave-particle interactions near the magnetospheric equator, on nearby magnetic field lines. The resulting diffuse aurorae pass electric fields and produce unstable gradients in the plasma density. The number and intensity of the falling charges

*Also at The European Space Agency Centre for Earth Observation, Frascati, Italy.
†Also at Department of Physics and Astronomy, University of Western Ontario, London, Ontario, Canada.
‡Also at Department of Physics and Engineering Physics, University of Saskatchewan, Saskatoon, Saskatchewan, Canada.
§Also at Department of Astronomy and Space Science, Korea University of Science and Technology, Daejeon, South Korea.

momentarily overwhelm the capacity of the lower ionosphere to extinguish the strong electric fields that follow from this action, spurring the growth of transient, turbulent electrojets, or Hall currents. In the 23 April 2023 case study, we establish a correlation between observations of chorus-wave activity near the magnetospheric equator and observations of turbulent electrojets in the ionosphere on closed magnetic field lines, from which we infer a causal chain where magnetospheric plasma waves ultimately drive small-scale turbulence in the ionosphere. We show how the predictions are brought to fruition in similar supporting events. Finally, we briefly discuss the implications that this discovery bears for the electrodynamics of the dayside ionosphere. In the following paper [M. F. Ivarsen, Phys. Rev. E **112**, 045203 (2025)] we follow the lengthy argument to a logical conclusion, leading to an alternative description of electrodynamics in the cusp region.

DOI: 10.1103/r6bv-pzlq

I. INTRODUCTION

The Sun's extended magnetic field, propagated by a constant wind of plasma originating from the Sun, naturally connects with Earth's own extended magnetic presence, the magnetosphere. The point of connection, or field integration, is referred to as reconnection. In general, this phenomenon powers a wide range of astrophysical processes by converting magnetic energy into kinetic energy.

In Earth's ionosphere, these processes are notably felt through the draining of electrons from the Van Allen belts into Earth's atmosphere [1], that is, electrons are given kinetic energy in a direction suitable to cause those particles to precipitate into the atmosphere, creating aurorae [2]. Importantly, reconnection also creates and maintains a giant twin-cell convection pattern that transports ionospheric plasma from the Sun-facing side of the ionosphere and into Earth's dark hemisphere, through the polar caps [3,4].

The above paragraph implies that the light and dark hemispheres of Earth's ionosphere are quite different. Energetic processes in the nightside ionosphere rely on hot (high-energy, or hard) electron populations in Earth's radiation belts as energy sources [5], with access to the hot electrons recently provided by nightside reconnection having in effect produced magnetic flux along closed magnetic field lines. The dayside ionosphere, on the other hand, is ionizaed largely due to sunlight and features a direct connection with the solar wind.

Near this connection point, called the cusp, dayside magnetic reconnection takes field lines that were previously closed and opens them up to the solar wind, allowing the precipitation of cold (low-energy, or soft) electrons into Earth's bright hemisphere, near the poles [6–9]. Regions of such soft electron precipitation frequently create poleward-moving auroral forms, aurorae that drift poleward from the cusp and into the polar cap along with the peeling off of magnetic flux from closed to open field lines [10–12].

The above notwithstanding, particle populations on closed field lines in the dayside magnetosphere are routinely powering energetic aurorae equatorward and eastward or westward of the cusp [13–15], in a manner equivalent to the nightside's mentioned energy source. The mechanism with which those electrons precipitate likewise involve pitch-angle scattering by wave-particle interactions [16]; for favored scattering angles, individual particles precipitate into the atmosphere [17,18].

In general, diffuse aurorae cause turbulence in the local plasma [19], for example, through plasma instabilities such as the gradient drift instability [20]. However, the strong electric fields that maintain instability growth depend on local electrodynamics. The dayside ionosphere is constantly being ionized by extreme ultraviolet radiation from the Sun, meaning that the electrical conductance of the plasma is generally elevated. The high ion mobility above 150 km altitude facilitates strong Pedersen currents that effectively short out electric field spikes by filling in positive charges, thereby negating the negative charges that precipitate. This action also works to destroy extant plasma irregularities faster [21,22].

On the other hand, in the nightside ionosphere, where conductance is low, the electric fields set up by the falling charges drive electrojet (Hall) currents [23], featuring intense turbulence (nonlaminar electrical currents) [24,25], observationally referred to as radar aurora [26].

The triggering of the instability processes that lead to such turbulent currents naturally depends on the plasma's conductivity. In sunlit conditions, the ionosphere is highly conducive to electrical currents (which move in the opposite direction of the falling auroral electrons), with the effect of shorting out electric fields. This is simply because nature will not allow the current continuity equation to be broken, largely proscribing the occurrence of intense turbulence in the sunlit high-latitude ionosphere [22] and providing motivation for our central research question: How can radar aurorae thrive on closed field lines in the strongly sunlit auroral ionosphere?

We demonstrate that diffuse aurorae on the dayside were driving turbulent electrojets during a major geomagnetic storm, triggered by the Farley-Buneman instability in the bottomside (the *E*-region) ionosphere, reacting to the relative ion-electron motion [27,28]. The structures are likely being seeded by gradient-drift waves breaking up. During an extensive case study, we demonstrate that the underlying cause behind these turbulent electrojets was wave-particle interactions and subsequent particle precipitation, produced near the equator in Earth's distant magnetosphere. We show that the predictions based on this case study are brought to fruition during the May 2024 superstorm, likewise in sunlit conditions over noon time Canada.

Importantly, the underlying mechanism, wave-particle interactions near the magnetospheric equator, have recently been demonstrated to have directly driven the near-instantaneous growth of Farley-Buneman turbulence on the nightside [29]; the present study is in that respect a natural extension of those findings to the dayside ionosphere on closed magnetic field lines. Here the phenomenon is both transient and its energy dissipation is highly localized, to the degree that it has largely eluded detection until now. In the

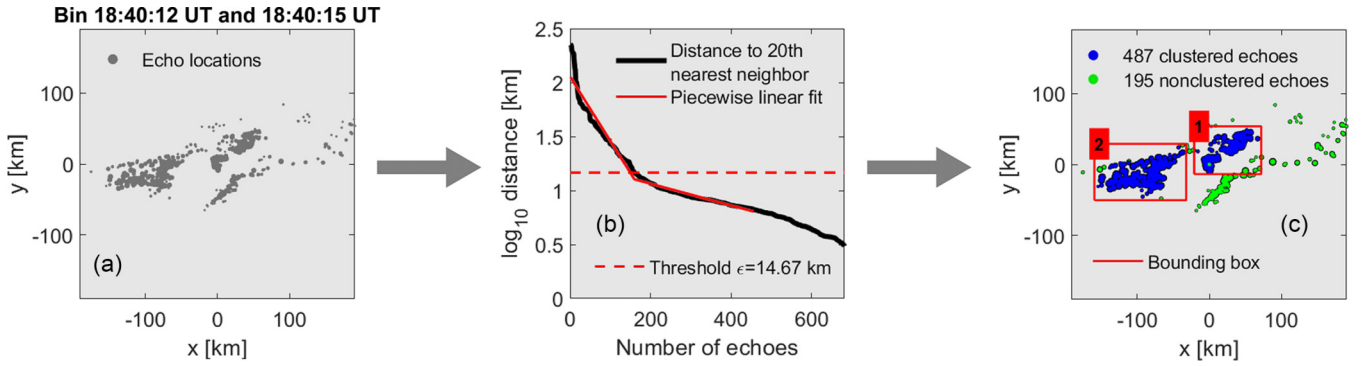

FIG. 1. Clustering of a 3-s ICEBEAR echo point cloud observed on 23 April 2023. (a) Raw echo locations. (b) A k-distance plot ($k = 20$), with a logarithmic y axis. A piecewise linear fit is shown with a red solid line, while the determined threshold value ϵ is indicated with a red dashed line. (c) Two clusters determiend with the `dbscan` algorithm using the threshold value $\epsilon = 14.67$ km and a nearest-neighbor value of $k = 20$. Bounding boxes are shown in a red solid line, clustered echoes in blue, and unclustered (noisy) echoes in green.

following paper [30] we follow the lengthy argument to a logical conclusion, namely, that closed field-line electrodynamics can power processes that have hitherto been the domain of dayside reconnection events.

II. METHODS

The present study relies on a series of datasets, and of these the core is made up of the ICEBEAR three-dimensional (3D) echo dataset.

The ICEBEAR radar is a continuous-wave coherent scatter radar [31], capable of imaging individual scattering regions (the spatial distribution of plasma turbulence), yielding 3D point-cloud radar data of ionospheric turbulence [32,33]. The origin of ICEBEAR's radar targets is tacitly assumed to originate in meter-scale Farley-Buneman waves in the unstable E region [27,28] as that instability is expected to crowd out any alternative mechanisms. The instability growth rates are largely perpendicular to Earth's magnetic field, and growth is subject to a sufficiently strong relative electron-ion drift [34]. By clustering and tracking the scattering regions, we are able to capture the motion of electric field source regions.

The main method with which we gain insights is the clustering and tracking of ICEBEAR radar echoes, a method expounded in Ref. [35], and which on average tracks ionospheric electric fields with striking fidelity [35,36]. We illustrate the method with a real-world example in Fig. 1.

Concisely, the method consists of four steps. For a point-cloud consisting of the raw, recorded echo locations (in a two-dimensional space perpendicular to Earth's magnetic field lines), the method is as follows.

(1) Calculate the nearest-neighbor distance between each point and its k nearest neighbors for all echo locations recorded inside a 3-s window.

(2) Find the leftmost kink in the k-distance curve, the point when the sorted nearest-neighbor distances reach a plateau. Points situated on this plateau are thought to be clustered. Points with a nearest-neighbor distance higher than this plateau are thought to be unclustered, or noisy. Find ϵ, the threshold distance value, with a piecewise linear fit of the k-distance curve.

(3) Apply the `dbscan` algorithm. This entails assigning points to clusters iteratively by requiring that the kth nearest neighbor of a point lies a distance less than ϵ away from that point.

(4) Clusters that are sufficiently similar from one time step to the next are considered to be the same. Since the number and orientation of the echoes within clusters are expected to change considerably in time, this test is performed simply through a comparison of the bounding boxes belonging to the clusters, rectangles that enclose the echoes inside a cluster, as well as the clusters' median (center-of-mass) echo locations. Compute five distance metrics: the longitudinal and latitudinal extent and location of the bounding box, and the median echo locations. Subtract the distance metrics between two potentially similar clusters. Then, if that subtraction yields distances that are all smaller than a threshold D, the two clusters are considered to be the same cluster.

The four steps are repeated for every clock second, meaning that each time bin exhibits 67% overlap with the neighboring bins. In the present paper we use $k = 20$ and $D = 8$ km [Fig. 1(b)], values that are appropriate for accurate spatial tracking of ICEBEAR echo clusters [35].

Next, in order to quantify the Hall drifts (the $\boldsymbol{E} \times \boldsymbol{B}$ drift implied by the apparent motion of the radar aurora), we must fit a linear polynomial to the successive echo center-of-mass values as a function of time within each track, that is, the displacement of the median echo location throughout an echo cluster's lifetime. These fits (performed in the longitudinal and latitudinal directions independently) exhibit slopes that quantify the cluster's apparent motion and are indicated with blue dashed lines in Fig. 2, which shows the time history of cluster 805 detected on 23 April 2023.

In the present paper we require that the variation in slope (quantified with 95% confidence intervals) be smaller than 2/3 of the slope magnitude. The efficacy of this method to identify and track ICEBEAR echo clusters, and its clear tendency to measure the ionospheric electric field have been demonstrated in Refs. [35,36], on whose record we rely. Returning to Fig. 2, we note that cluster 805 appeared to move northeastward with a considerable velocity of approximately 3200 m/s.

In addition to ICEBEAR, in the present study we rely on data from two U.S. climate satellites, the Japanese magnetospheric

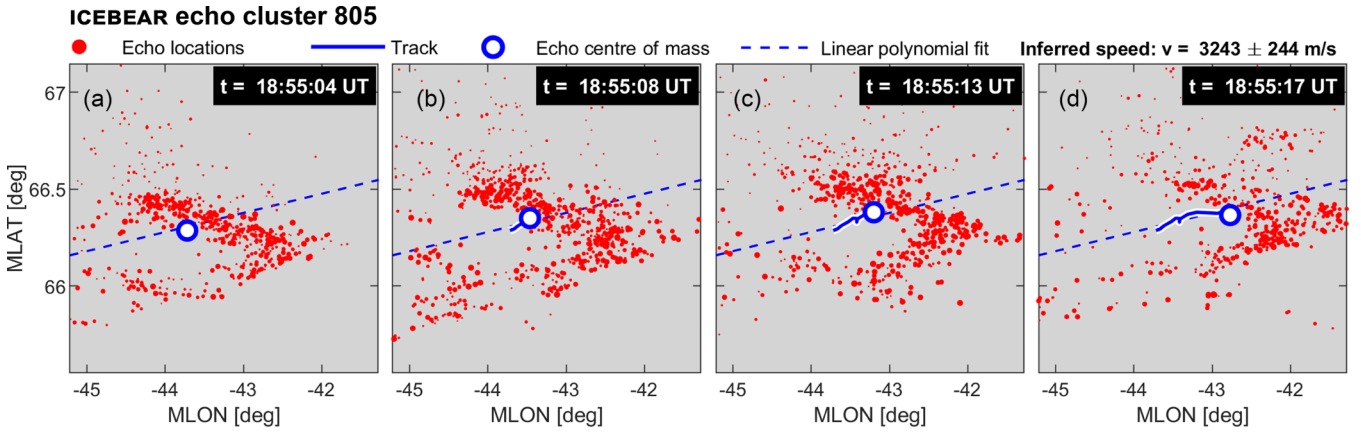

FIG. 2. Time history of a particular superfast ICEBEAR echo cluster that was identified and tracked around 18:55 UT, identified as cluster 805. Each of the four panels shows a 3-s snapshot in the life of that cluster. Individual echoes are shown with red points. The spatial track is shown with a blue solid line, while a linear polynomial fit to the motion is shown with a blue dashed line. The echo cluster's inferred speed (approximately 3200 m/s) is indicated. We note that the echo cluster was observed wholly within ICEBEAR's field of view and that appreciable backscatter power is expected throughout the region enclosed by the axes. For cluster 805's echo altitude distribution, see Fig. 9.

spacecraft Arase, the international SuperDARN radar network, and the Canadian CHAIN network of GPS receivers, to be introduced in the next section.

III. RESULTS

The present study is centered around an event that took place near the ionospheric cusp during a major geomagnetic storm on 23 April 2023. Figure 3 briefly summarizes the conditions of geospace before and during the storm. As the storm commenced (17:35 UT), the solar wind dynamic pressure started oscillating, perhaps indicative of bow shock ripples and subsequent high-speed jets [38], an important source of free energy for the dayside ionosphere on closed field lines [39]. The interplanetary magnetic field B_Z component started a descent towards –25 nT, while the B_Y component oscillated around 0 nT with a rather large amplitude. For other, detailed, plots of the interplanetary magnetic field during this particular geomagnetic storm, see, e.g., Fig. 1 in Ref. [40], Fig. 1 in Ref. [41], or Fig. 1 in Ref. [42].

As the storm was commencing, the province of Saskatchewan in Canada, the region of interest in the present study, moved with Earth's rotation into the noon sector, bringing with it the field of view of the ICEBEAR radar, a local SuperDARN radar, and a CHAIN GPS receiver.

Two fortunate and disparate space-ground conjunctions subsequently took place during the storm's main phase, allowing us to infer the exact conditions in and around ICEBEAR's field of view. First came the U.S. National Oceanic and Atmospheric Administration (NOAA) polar orbiting climate satellite, NOAA-18. Figure 4 summarizes the conjunction event. The satellite's onboard particle detectors observed a sharp increase in the soft (50 eV to 1 keV) electron energy flux, coincident with a localized, strong ion energy flux, at 67.7° magnetic latitude (MLAT). This observation is a local signature of the ionospheric cusp [8,45]. At the same time, the abrupt change in the trapped electron flux at 18:37:30 UT is a signature of the open-closed field-line boundary (OCB) [46]. Comparing Figs. 4(a) and 4(d), we conclude that the radar echoes were observed just equatorward of the open-closed field-line boundary and thus on closed magnetic field lines.

Meanwhile, the Japanese inner-magnetosphere spacecraft Arase orbited Earth at a distance of around 5 Earth radii, just south of the magnetic equator in the dayside inner magnetosphere [47]. During the event, Arase's northern hemisphere ionospheric footprint was mapping southeast of ICEBEAR's field of view, shown in Fig. 5(a). Also on display in that

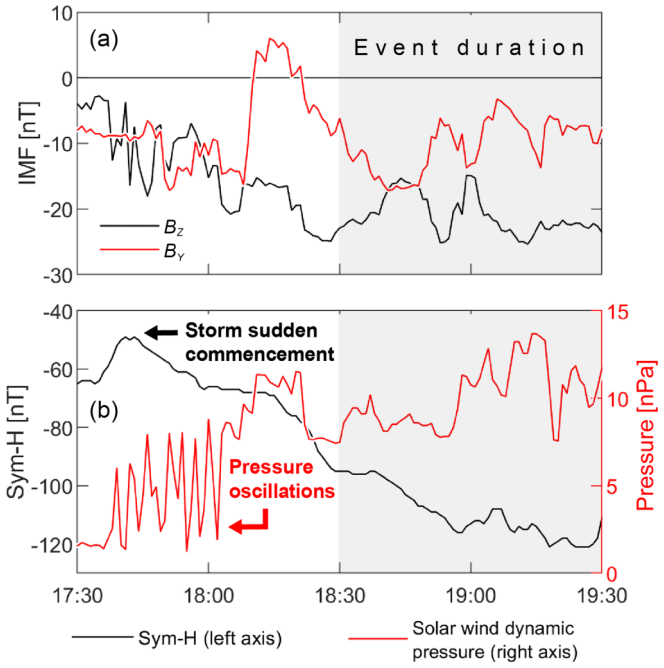

FIG. 3. Solar wind parameters and geomagnetic activity index values for the interval from 17:30 UT to 19:30 UT on 23 April 2023. A gray shaded area denotes the duration of the event under study. (a) Interplanetary magnetic field (IMF) B_Z (black) and B_Y (red) components time shifted to the bow shock [37]. (b) Sym-H geomagnetic storm index (black left axis) and solar wind dynamic pressure (red right axis).

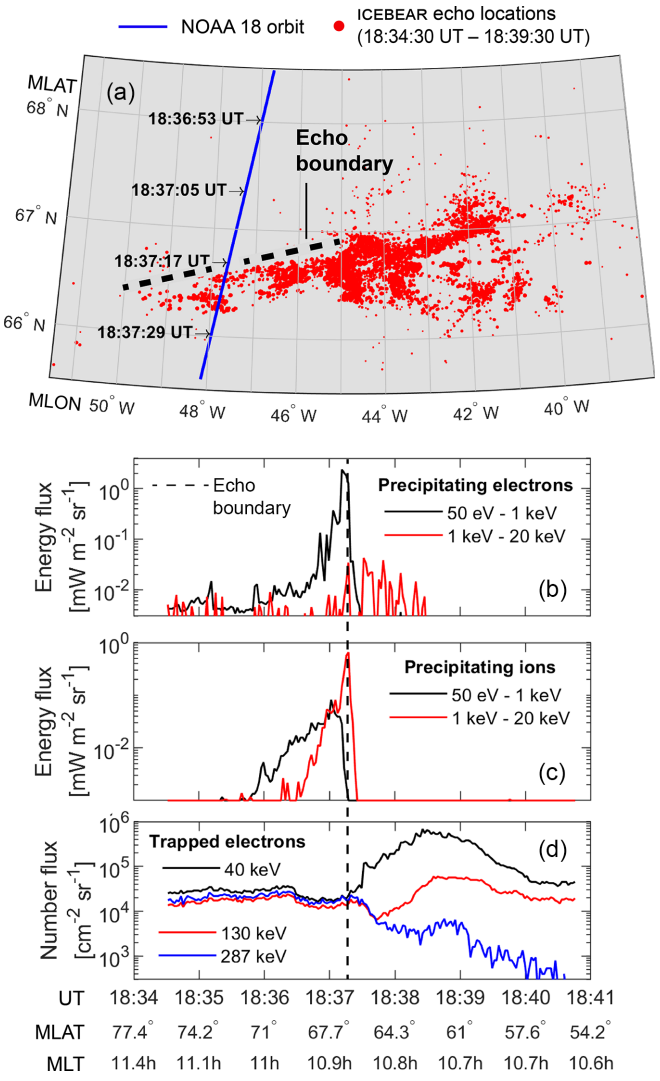

FIG. 4. Observations made by the NOAA-18 spacecraft [43] of precipitating (b) electrons and (c) ions, using the TED 0° telescope, and (d) trapped electrons, using the medium-energy proton and electron detector 30° telescope [44]. In (b) and (c), black and red lines indicate low- and high-energy particles, respectively, while (d) shows three distinct high-energy populations. (a) Point cloud of ICEBEAR echoes, as observed between 18:34:30 UT and 18:39:30 UT. The orbital footprint of NOAA-18 is superposed, where we trace the orbital footprint along magnetic field lines from an altitude of 850 km. The boundary that separates the regions with and without ICEBEAR echoes is indicated in all panels with a black dashed line.

figure are data from SuperDARN, a global network of coherent scatter radars that provide Doppler shifts of drifting *F*-region plasma, reflecting the magnetospheric plasma convection. A global data assimilation model provides estimates of this pattern at 2-min cadence. Figure 5(a) plots the global convection estimate as a collection of thin black arrows.

Coincident with the space-ground conjunction, ICEBEAR saw echo cluster motions that consistently moved poleward and eastward. In Fig. 5(a) we show with a thick black arrow the mean cluster velocity observed between 18:30 UT and 19:15 UT. A thick yellow arrow denotes the mean electric field $\boldsymbol{E}$ inferred from the echo cluster motion: $E = \boldsymbol{B} \times \boldsymbol{v}$, with $\boldsymbol{B}$ the magnetic field [modeled using the International Geomagnetic Reference Field (IGRF) [50]] and $\boldsymbol{v}$ the apparent cluster motion [36].

In Fig. 5(b) we show observations made by Arase in the inner magnetosphere that elucidate and substantiate our inferences. During and prior to the event, Arase observed an elevated flux of high-energy (20–60 keV) electrons at pitch angles lower than 10° from a position of around −20° MLAT in the southern hemisphere just outside the plasmasphere, and the satellite also registered intense whistler-mode waves outside the plasmapause; we show this in Fig. 6. The chorus-wave-particle interactions in Fig. 6(b) would lead to pitch-angle scattering and subsequent electron precipitation. As such, based on Fig. 6, we infer that a substantial part of the electron flux in Fig. 5(b) precipitated into the northern hemisphere near ICEBEAR's field of view. The flux of electrons subsides from 19:20 UT as the satellite's orbital footprint leaves the theater.

To relate the observations to auroral pulsations, an absence of optical observations notwithstanding, we present in Fig. 6 a timescale analysis of the magnetic field fluctuations observed with the plasma wave experiment (PWE) instrument on board Arase [51,52]. Figure 6(a) shows wave fluctuations in the lower chorus band and Fig. 6(b) shows the periodicities present in these time series. We observe profuse oscillations that peak (during the interval) at 12–13 s. This peak coincides with the most probable duration of the superfast turbulent Hall drifts seen by ICEBEAR.

Summary of results

Seen together, the many complicated conjunctions support two main observations: (i) A multitude of echoes from the radar aurora occurred at magnetic noon, on closed magnetic field lines and in the immediate vicinity of the open-closed field-line boundary (Fig. 4) and (ii) the rate of echo production was driven by high-energy particle precipitation caused by chorus waves near the radiation belts (Figs. 5 and 6).

IV. DISCUSSION

A. High-energy diffuse aurorae as drivers of Farley-Buneman turbulence

We were then left with aurorae that were immersed in a vast sunlit soundscape of ultralow-frequency waves [53], some of which we infer to have produced pulsating auroral patches [54]. We were unable to observe the aurorae directly, but we infer that they shone, invisibly, in characteristic patterns, thereby modulating the electric and density fields [55,56], in turn creating gradient-drift unstable seeds of ionization in the ionosphere [20]. These kilometer-scale irregularities came with the structured polarization electric field necessary to drive intense small-scale turbulence, fields that were ultimately provided by the falling charges.

We base this narrative on Figs. 5 and 6, the first of which shows the echo detection rate against integrated electron number flux after shifting the former around 6 min forward in time. The two time series there exhibit matching fluctuations during a 24-min interval, before the satellite orbited out of the active region. As great uncertainty surrounds the exact field-aligned

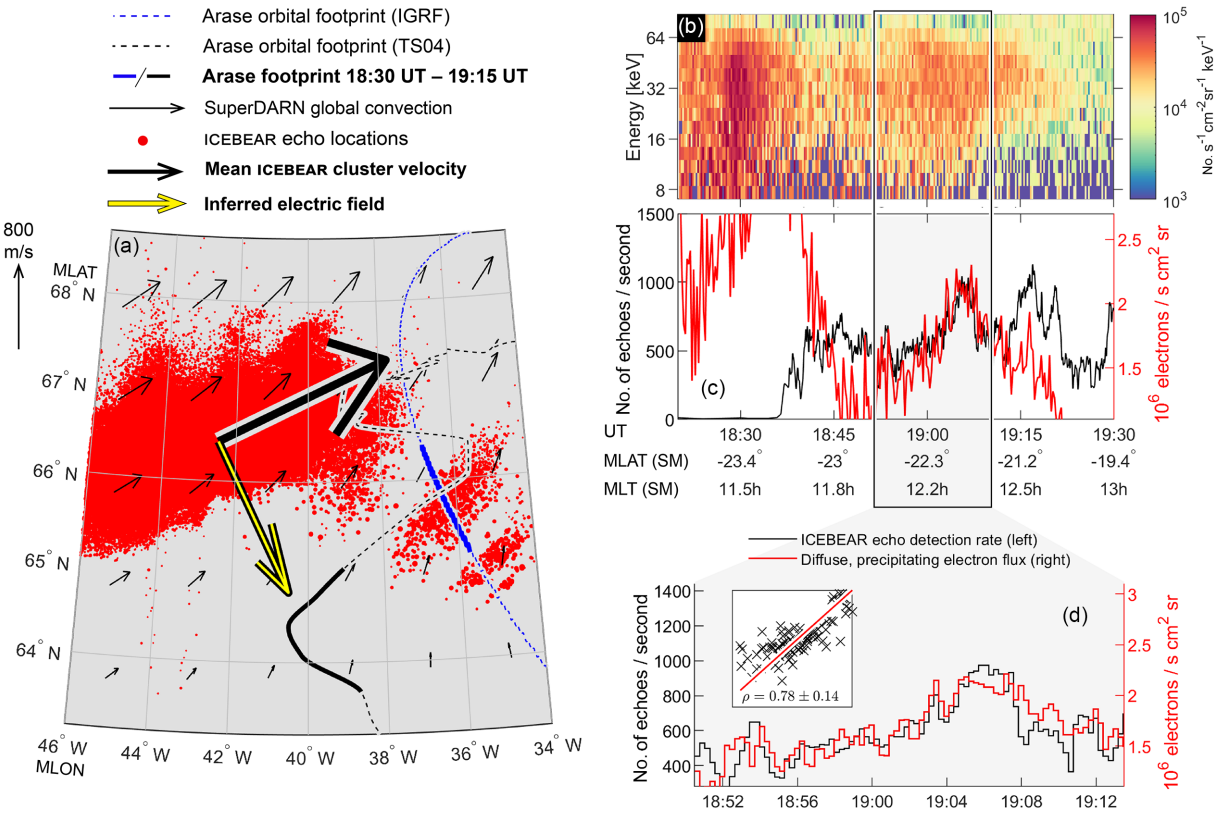

FIG. 5. (a) SuperDARN global convection as thin black arrows, superposed on the point cloud of ICEBEAR echoes observed between 18:30 UT and 19:15 UT (red dots). Thin blue and black dashed lines indicate the orbital footprint of Arase, with thick lines showing the mentioned interval. We trace Arase's highly elliptical orbit (apogee 32 000 km, inclination 31°) to ionospheric altitudes using the IGRF (blue) and TS04 (black) models. A thick black arrow shows the weighted (by number of echoes) mean cluster velocity observed in the ICEBEAR point clouds, drawn at scale (around 1500 m/s in magnitude). A yellow arrow shows the (45-min) average electric field inferred from that motion (82 mV/m). (b) Electron particle flux for pitch angles lower than 10°, for particle energies between 7 and 87 keV, measured by Arase between 18:20 UT and 19:30 UT [48]. (c) Comparison of the ICEBEAR echo detection rate (shifted 5.5 min forward in time and smoothed with a 16-s Savitsky-Golay filter, black left axis) against the integrated precipitating number flux (red right axis). The x axis below (c) shows time in UT on 23 April 2023, as well as magnetic latitude and local time in solar magnetic coordinates. (d) Enlargement of an approximately 20-min interval from (c). The Pearson correlation coefficient between the time series ($\rho = 0.78$) is indicated with an inset linear regression. We note that there is a considerable difference between the mapping techniques in Arase's orbital footprint, and the magnetosphere had undergone a rather extreme contraction; the coincident space-ground conjunction is therefore partly determined through the strong correlation between the time series [49]. For an ionization rate altitude profile based on the Arase observations, see Fig. 9.

mapping of Arase's footprint, the clear association between the precipitating energy flux and the detection of ICEBEAR echoes tells us that the two instruments, though separated by several Earth radii, responded to the same signal.

The temporal shift of around 6 min is likely accounting for a large latitudinal separation between the observations (6 min of 600-m/s drift corresponds to a distance of 216 km, or 2° in latitude). An explanation follows.

1. *Large latitudinal separation between Arase and the Hall current channels*

In Fig. 5(a) the latitudinal distance between Arase's ionospheric footprint and the observed turbulent Hall channels exceeds several hundred kilometers. A large distance notwithstanding, the observed particle precipitation likely covered a large region of space, as is typical for diffuse aurorae [57], and the observations may have been made on opposite sides of the same diffuse collection of patches. Furthermore, Figs. 5(b)–5(d) detail the matching temporal characteristics of the radar aurorae and the observed particle flux, exhibiting a strong Pearson correlation coefficient (0.78).

This is only after shifting the precipitation data backward by 5.5 min, but association is strengthened by the matching of several peaks between the two signals. This correlation and the clear association in Fig. 6 strongly indicate a causation that can go either way, and, *reductio ad absurdum*, this causation can only go one way: from the magnetosphere to the E region. The third option, that both signals are dependent on a common external cause, is unlikely all the while that the ICEBEAR observations took place on closed magnetic field lines, after the magnetospheric observations.

2. *Identified driver: Chorus-wave activity*

Figure 6 identifies the common driver of the two signals. There a periodicity of around 12 s is observed in both time series, in line with expectations for pulsating aurorae [58,59],

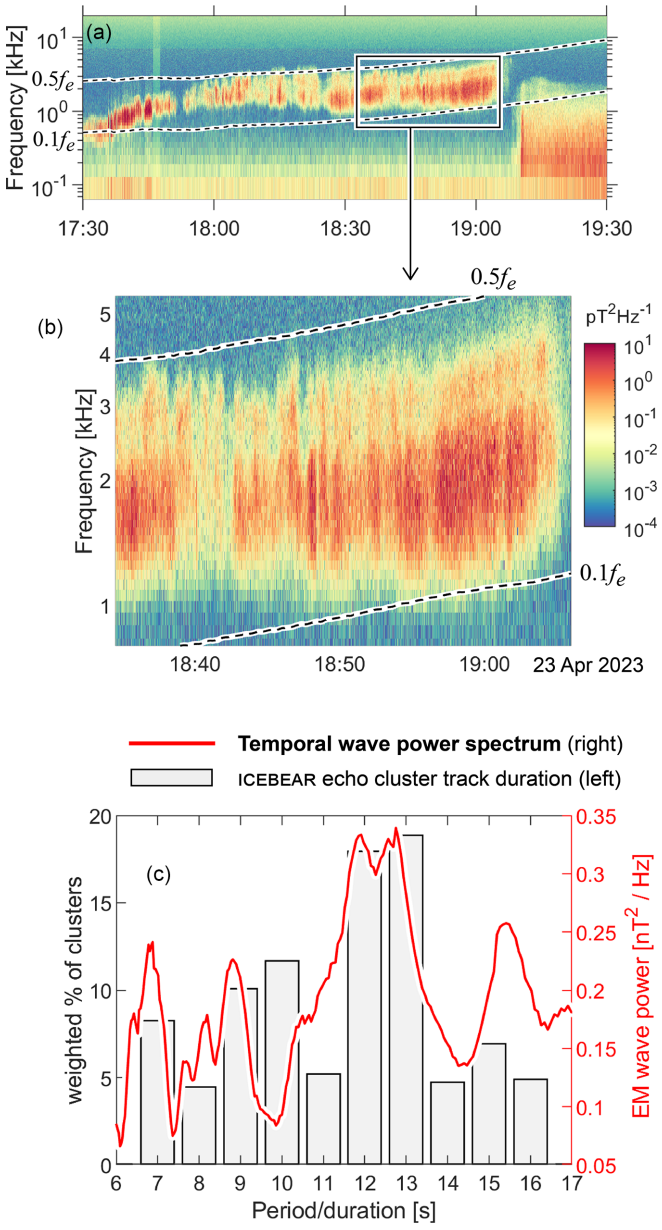

FIG. 6. (a) and (b) Lower-band chorus-wave magnetic field fluctuations measured by the PWE instrument on board Arase, with the frequencies $0.1f_e$ and $0.5f_e$ (f_e being the electron cyclotron frequency) indicated. (c) Shown in gray is the echo-weighted track durations (the number of seconds that an echo cluster was successfully tracked), observed during the same interval as in (b). Note that only an additional three clusters were tracked that lasted longer than 17 s during the interval; these are omitted from the plot and we focus on the time interval expected for chorus-wave oscillations. Superposed, a red line shows the oscillation frequencies of the lower-band chorus waves (the power spectrum of a time series of the root-mean-square integration of the magnetic field spectra for frequencies between $0.1f_e$ and $0.5f_e$).

and the lower-band chorus waves we observe in Figs. 6(a) and 6(b) adhere to this expectation. Periodic electric field bursts associated with pulsating auroral patches could then explain why echo clusters were tracked for an average of 12 s each.

3. Additional evidence

The discovery of severely turbulent Hall currents in the dayside E region equatorward of the cusp, on closed magnetic field lines, is new, or at least directly dependent on data that are severely lacking in the literature. To provide further evidence for this discovery, we have analyzed two additional, fortuitous space-ground-ground conjunctions. Both took place on 10 May 2024, during the most severe geomagnetic storm to occur in geospace in two decades. As ICEBEAR's field of view rotated into the noon sector on that day, two of NOAA's climate satellites orbited overhead, directly through the cusp region. Figure 7 shows both conjunctions. The first (six panels of the left column) took place on 18:00 UT, while the second (six panels of the right column) took place 40 min later. During both conjunctions, we identify the OCB in the trapped electron flux [Figs. 7(e) and 7(h)]. Conferring with the distribution of ICEBEAR echoes [Figs. 7(a) and 7(b)], we conclude that the bulk of the echoes were detected directly equatorward of the cusp, on closed magnetic field lines. Furthermore, through clustering and tracking of the echo data, we found several transient, superfast clusters of echoes, moving primarily eastward, with speeds that far exceeded the SuperDARN-modeled global convection and with directions that skewed considerably more eastward than the global convection would indicate.

Although we were not able to find evidence of diffuse high-energy aurorae during the two additional conjunctions that took place on 10 May 2024, we can readily infer conditions that are fundamentally similar to the main event under study in the present paper. More specifically, on closed magnetic field lines, equatorward of the cusp, we observe fast eastward motions that are inconsistent with observations of F-region plasma convection and which are highly consistent with strong enhancements to the local electric field in the E region. The implications are that, during severe geomagnetic disturbances, transient eastward motions are expected equatorward of the cusp on closed magnetic field lines.

B. Nonlinear route through ionization and penetrating electric fields

Having, with Figs. 4–6, established a clear correlation between chorus-wave-induced diffuse aurorae in the magnetosphere and the occurrence and motion of radar aurorae in the E region, we now elucidate the physical causal path between the two phenomena that we briefly mentioned above, a causal chain that we illustrate in Fig. 8. In so doing, we will additionally analyze coincident GPS scintillations observed in association with the event under study.

In Fig. 8 the combined electric field and density gradient ultimately drive the trigger for several-meter-sized Farley-Buneman waves, through the generation of ionization seeds and attendant electric field modulations.

1. Supporting evidence: GPS scintillations

In support of the argument, consider Fig. 9, which shows observations of echo cluster 805, in direct proximity of GPS

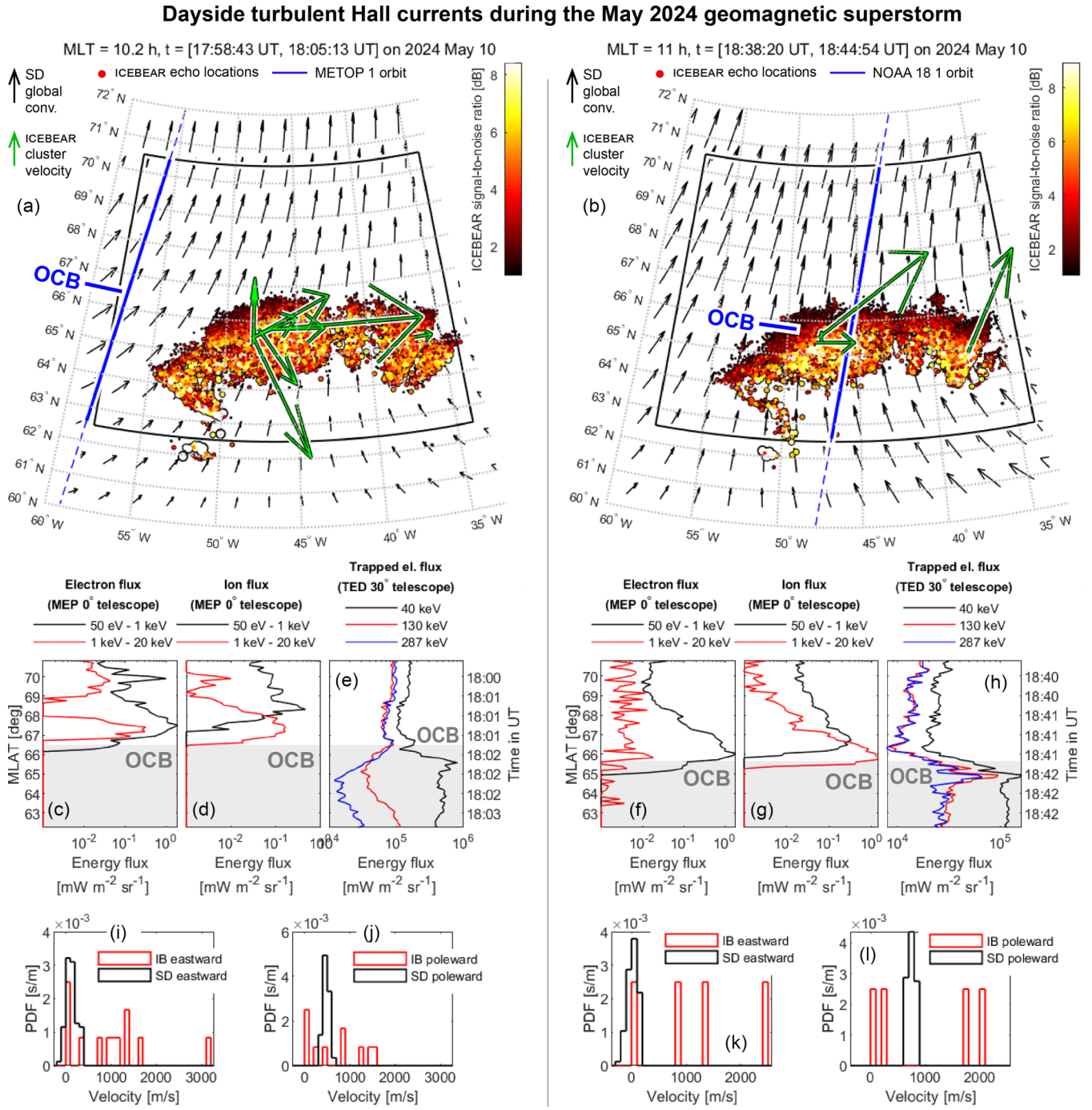

FIG. 7. Two space-ground conjunctions between ICEBEAR, SuperDARN, and the METOP-1 (left) and the NOAA-18 (right) satellites, respectively. (a) and (b) Satellite orbit (blue line) superposed on the globally modeled plasma convection (thin black arrows), ICEBEAR echo locations (color-coded dots, black-red-yellow-white color scheme), and the ICEBEAR cluster velocities recorded during the conjunction (green arrows). (c)–(h) *In situ* satellite observations of extant particle fluxes, from the MEP and TED instruments. A gray shaded region indicates the part of the orbit that corresponds to closed magnetic field lines; the abbreviation OCB indicates the location of the open-closed field-line boundary in (a)–(h). (i)–(l) Histograms of the observed ICEBEAR cluster velocities in the (i) and (k) eastward and (j) and (l) poleward directions (red), compared to the modeled SuperDARN velocities inside the region of interest. Note that the leftmost conjunction (METOP-1) did not take place directly adjacent to the distribution of ICEBEAR echoes and a cusp signature is not evident; the conjunction can nevertheless identify the location of the OCB in (e).

scintillations seen in a CHAIN GPS receiver [62] situated directly beneath ICEBEAR's field of view (see also Figs. S1–S3 in the Supplemental Material [63] for three additional, fundamentally similar, comparisons).

Figures 9(b) and 9(c) show the altitude distributions in both echo locations and an Arase-derived ionization altitude profile, compared to the various GPS pierce point altitudes. A sample cross-correlation analysis between the ICEBEAR echo

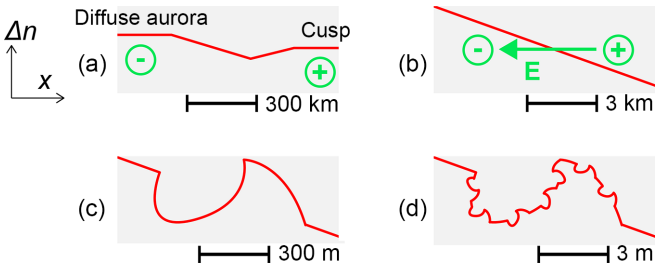

FIG. 8. (a) Schematic representation of the ionosphere equatorward of the cusp, near or along the OCB; for a nuanced discussion of the specific charge deposition associated with the equatorward edge of the cusp, see the following paper [30]. (b) Energetic particle impact produces ionization, leading to plasma density gradients Δn perpendicular to the precipitation-induced electric field E. (c) The combined electric field and density gradient drive the gradient-drift instability, generating hundreds of meter-scale turbulent structures. These structures decay and lead to the generation of secondary waves. (d) When the electron-ion drift velocity exceeds the ion-acoustic speed, the seeds will trigger the several-meter-sized Farley-Buneman instability, which in addition feature a component rotated away from the ambient electric field).

detection rates and the GPS signal amplitudes reveals that a temporal shift of +5 s is in order, after which the time series exhibit a strong correlation $\rho = 0.72$ [Fig. 9(e)], implying that, regardless of any other inferences, the GPS-scintillation pierce point should be located just downstream from the moving echo cluster.

Comparing Figs. 9(a) and 9(b), we observe that the *F*-region pierce points are located far away from the echo cluster, seemingly incompatible with a 5-s (approximately 16 km) shift. Assuming a pierce point altitude of around 100 km, however, places the pierce point roughly at the location of the echo cluster and near the most likely altitude with highest ionization rate (90 km). The ICEBEAR echoes in Fig. 9 exhibited a median altitude of 97 km. The implication is that the GPS scintillations took place in the *E* region. While the data do not present definite proof of this inference, we note recent comprehensive studies that strongly favor the *E* region as the layer of auroral GPS scintillations rather than the *F* region [64].

2. *Causality*

An argument for causality follows. As we have shown in the preceding section, diffuse aurorae occupied the region equatorward of the theater. The aurorae pass electric fields and cause impact ionization, leading to, among other thing, unstable plasma density gradients [20]. Aided by the induced perpendicular electric fields, the gradient-drift instability (GDI) will develop, likely primarily in the *F* region, where it is commonly associated with high-latitude GPS scintillations [65–67], and to a lesser degree, in the *E* region. Gradient-drift waves end up seeding Farley-Buneman turbulence in the *E* region (Fig. 8).

The formation of the seed mechanism, the GDI waves, is primary expected in the *F* region. There the difficulties of developing instabilities in the lower *E* region, owing to ion-neutral collisions, can retard the growth. However, regardless of the exact region in which the instability develops, the GDI waves would cause both turbulent cascades and secondary waves. The following field perturbations would be felt in the lower *E* region, owing to a very long field-aligned wavelength associated with the density perturbations, as well as field-aligned transport (see Fig. B1 in Ref. [19]). We therefore ascertain with some confidence that the gradient-drift waves ultimately acted in this way as seeds for the Farley-Buneman instability.

In the ICEBEAR 3D dataset, there is a clear tendency for echoes to cluster tightly in structures around 2–5 km in size [33,68,69]. This otherwise highly surprising result is in direct support of the above chain of argument.

The full causal chain thus involves wave-particle interactions causing electrons to precipitate, thereby embedding a characteristic spatiotemporal pattern of ionization and electric field modulations in the ionosphere. This pattern spurs the growth of turbulence, which eventually seeds Farley-Buneman waves. The physical route was recently demonstrated in action, presented in a recent clear-cut case study [29].

3. *Comment on magnetohydrodynamics*

The conventional view of ionospheric dynamics holds that the motion of plasma, driven by magnetic reconnection, drives field-aligned and -perpendicular electrical currents, in adherence to the principles of MHD. While we do not dispute the validity of the foregoing sentence, we must point out the idealized nature of this description. Aurorae are frequently driven by kinetic wave-particle interactions in Earth's radiation belts, providing nuance to the above statement that current systems are set up and maintained by the motion of plasma. The Pedersen currents, which according to the idealized MHD view are caused by the vorticity around field-aligned currents, are carried by ions and naturally point towards the deposition of negative charges. In other words, it is the same fields that appear due to the vorticity of the current systems that are evoked in the present article to neutralize the excess charges introduced by particle precipitation and which are observed by their attendant turbulent Hall drifts.

The infrastructure needed for the magnetohydrodynamic current generator has therefore already been precipitated by kinetic wave particle interactions, processes that are not directly reflecting the ongoing rate of reconnection with the solar wind.

V. SUMMARY AND FUTURE OUTLOOK

The present paper is concerned with documenting and substantiating a clear causal path from the drivers of dayside diffuse aurorae to the production of Farley-Buneman turbulence in the unstable *E* region just equatorward of the cusp. To this end, we have relied on extensive analysis of the conjunction of five ground- and space-based sources of data, all collected over Canadian geospace during the onset of the 23 April 2023 geomagnetic storm.

We observed profuse radar aurorae equatorward of the cusp (Fig. 4) that carried clear signatures of chorus-wave-induced high-energy particle precipitation (Figs. 5 and 6). The diffuse

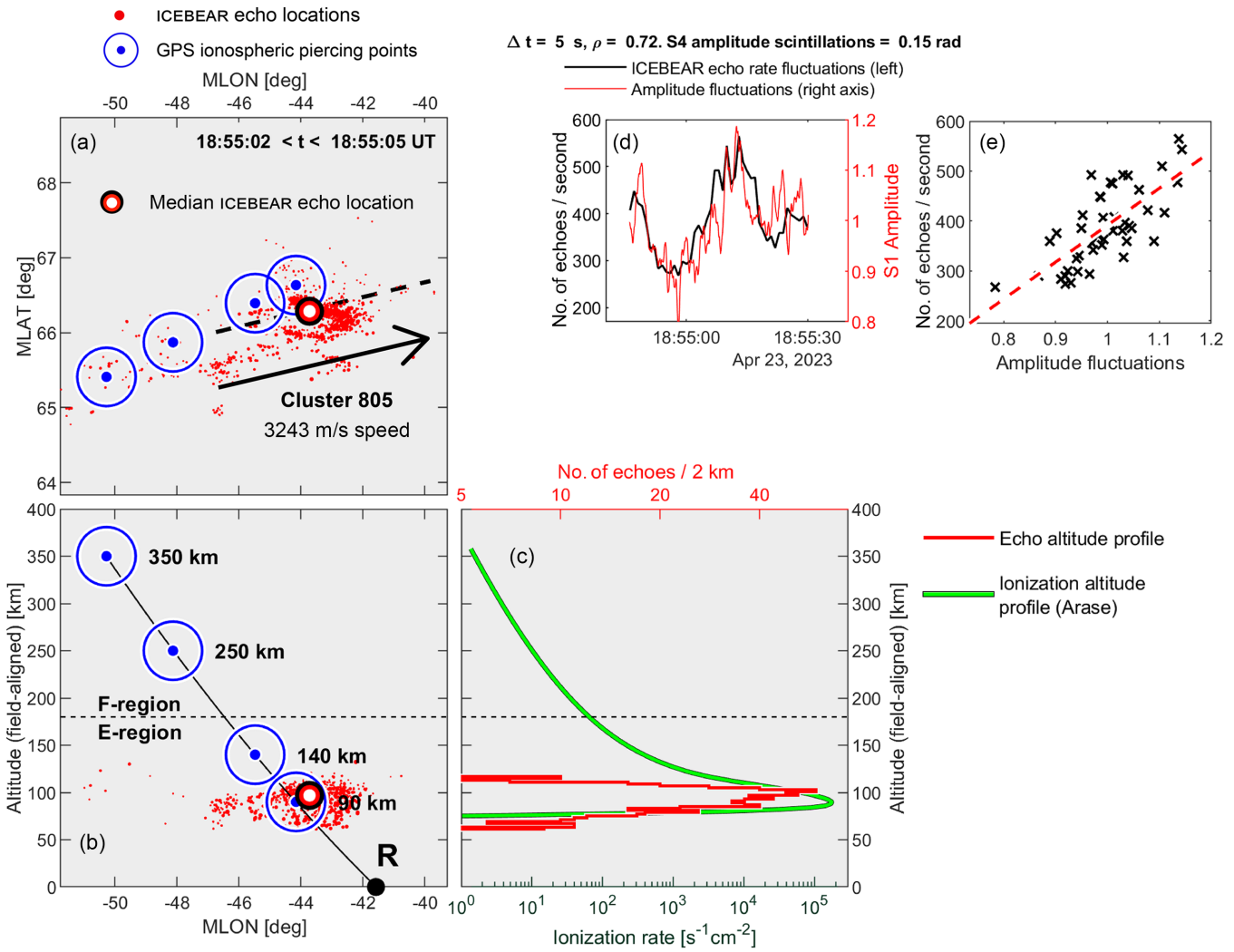

FIG. 9. Ground-ground conjunction between ICEBEAR and GPS scintillations observed in the receivers on the ground below the radar field of view, from the Rabbit Lake research station. (a) and (b) A 3-s snapshots during the event, both (a) in the plane perpendicular to Earth's magnetic field and (b) projected onto the vertical (field-aligned altitude), affording a full 3D view of the situation. The distribution of ICEBEAR echoes is represented by red dots, the median location is indicated with a thick red circle, and the echoes' apparent motion is indicated with a black arrow. Bull's-eye symbols gives the position of the scintillation ionospheric pierce points for altitudes between 90 and 350 km. The receiver location is marked with **R**, and a black line connects the receiver to the various (hypothetical) pierce points in the ionosphere. (c) Ionization rate altitude implied by the particle flux in Fig. 5(b), using the methodology in Ref. [60] for a flux conversion from number to energy and then the parametrizations by Ref. [61] to calculate ionization rate altitude profiles (green). The altitude distribution of the ICEBEAR echoes observed during this 3-s interval is superposed in red. (d) GPS signal amplitude fluctuations (red right axis, smoothed with a 3-s Savitsky-Golay filter) and the ICEBEAR rate of echo detection (black left axis), with a temporal shift of 5 s applied to the former. (e) Comparison of the echo rates with the amplitude fluctuations in a scatterplot, with a linear regression indicated by a red dashed line. Echo cluster 805 is likewise the subject of Figs. 4(c)–4(f). Similar examples recorded during the event under study are provided in the Supplemental Material [63].

aurorae produced ionization and passed electric fields, fueling instabilities over a wide range of scales (Fig. 9), eventually seeding the Farley-Buneman instability and the subsequent detection of widespread *E*-region radar echoes on closed magnetic field lines. Wave-particle interactions are in this way directly driving small-scale turbulence, using a physical causal chain that was recently demonstrated to occur in the nightside ionosphere [29], and the predictions were brought to fruition in space-ground conjunctions that took place during the May 2024 geomagnetic superstorm.

The meticulous approach is necessitated by a lack in the literature of established turbulent phenomena in the dayside high-latitude *E* region on closed magnetic field lines. Observations of dayside auroral electrojets are sparse, but not without precedence [70].

The implications are that transient, turbulent Hall currents may be excited in the dayside high-latitude ionosphere during severe geospace disturbances. In fact, the mechanism we evoke has been suggested by Ref. [71] as an anomalous cause of poleward-moving auroral forms. Observations of the latter are almost invariably tied to pulsed dayside reconnection events, in stark contrast to high-energy particle precipitation from the dayside magnetosphere. Any alternative mechanism producing fast motions near the cusp must therefore be subject

to close scrutiny, and in the following paper [30] we carefully discuss the eventuality.

ACKNOWLEDGMENTS

This work was supported in part by the European Space Agency (ESA) Grant No. 1000012348 and by the Research Council of Norway Grant No. 324859. We acknowledge support from the Canadian Space Agency (Grant No. 20SUGOICEB), the Canada Foundation for Innovation John R. Evans Leaders Fund (Grant No. 32117), the Natural Science and Engineering Research Council, the Discovery grants program (No. RGPIN-2019-19135), the Digital Research Alliance of Canada (Grant No. RRG-4802), and basic research funding from Korea Astronomy and Space Science Institute (Grant No. KASI2024185002). M.F.I. is thankful to R. Thorne and L. Clausen for stimulating discussions and to S. Matsuda, K. Keika, T. Hori, and M. Teramoto for data handling.

DATA AVAILABILITY

Science data of the ERG (Arase) satellite were obtained from the ERG Science Center operated by ISAS/JAXA and ISEE/Nagoya University [72]. This includes Lv.3 MEPe [48], Lv.2PWE/OFA [73], Lv.2 PWE/HFA [51], and Lv.2 MGF [74]. ICEBEAR 3D echo data are available from [31,32,75]. SuperMAG data can be accessed from [76]. Solar wind data from NASA's OMNI service can be accessed from [77]. SuperDARN data were processed using RST with the FITACF 3 algorithm, order/degree 6, the empirical model from [78], downloadable using Globus [79]. NOAA-18 data are available from [80].

[1] R. M. Thorne, B. Ni, X. Tao, R. B. Horne, and N. P. Meredith, Scattering by chorus waves as the dominant cause of diffuse auroral precipitation, Nature (London) **467**, 943 (2010).

[2] S. Kasahara, Y. Miyoshi, S. Yokota, T. Mitani, Y. Kasahara, S. Matsuda, A. Kumamoto, A. Matsuoka, Y. Kazama, H. U. Frey, V. Angelopoulos, S. Kurita, K. Keika, K. Seki, and I. Shinohara, Pulsating aurora from electron scattering by chorus waves, Nature (London) **554**, 337 (2018).

[3] T. Iijima and T. A. Potemra, Large-scale characteristics of field-aligned currents associated with substorms, J. Geophys. Res. **83**, 599 (1978).

[4] S. W. H. Cowley, in *Magnetospheric Current Systems*, edited by S.-I. Ohtani, R. Fujii, M. Hesse, and R. L. Lysak, Geophysics Monograph Series, Vol. 118 (American Geophysical Union, Washington, DC, 2000), p. 91.

[5] P. T. Newell, T. Sotirelis, and S. Wing, Diffuse, monoenergetic, and broadband aurora: The global precipitation budget, J. Geophys. Res. **114**, A09207 (2009).

[6] M. Saunders, The polar cusp ionosphere: A window on solar wind–magnetosphere coupling, Antarctic Sci. **1**, 193 (1989).

[7] G. G. Shepherd, Dayside cleft aurora and its ionospheric effects, Rev. Geophys. **17**, 2017 (1979).

[8] P. T. Newell and C.-I. Meng, The cusp and the cleft/boundary layer: Low-altitude identification and statistical local time variation, J. Geophys. Res. **93**, 14549 (1988).

[9] Y. Ogawa, R. Fujii, S. C. Buchert, S. Nozawa, and S. Ohtani, Simultaneous EISCAT Svalbard radar and DMSP observations of ion upflow in the dayside polar ionosphere, J. Geophys. Res. **108**, 1101 (2003).

[10] H. U. Frey, D. Han, R. Kataoka, M. R. Lessard, S. E. Milan, Y. Nishimura, R. J. Strangeway, and Y. Zou, Dayside Aurora, Space Sci. Rev. **215**, 51 (2019).

[11] D. J. Southwood, C. J. Farrugia, and M. A. Saunders, What are flux transfer events? Planet. Space Sci. **36**, 503 (1988).

[12] K. Oksavik, J. Moen, and H. C. Carlson, High-resolution observations of the small-scale flow pattern associated with a poleward moving auroral form in the cusp, Geophys. Res. Lett. **31**, L11807 (2004).

[13] M. Spasojevic and U. S. Inan, Drivers of chorus in the outer dayside magnetosphere, J. Geophys. Res. **115**, A4 (2010).

[14] B. Ni, J. Bortnik, Y. Nishimura, R. M. Thorne, W. Li, V. Angelopoulos, Y. Ebihara, and A. T. Weatherwax, Chorus wave scattering responsible for the Earth's dayside diffuse auroral precipitation: A detailed case study, J. Geophys. Res. **119**, 897 (2014).

[15] H. Feng, D. Wang, D. Guo, Y. Y. Shprits, D. Han, S. Teng, B. Ni, R. Shi, and Y. Zhang, Lower band chorus wave scattering causing the extensive morningside diffuse auroral precipitation during active geomagnetic conditions: A detailed case study, J. Geophys. Res. **129**, e2023JA032240 (2024).

[16] Y. Nishimura, J. Bortnik, W. Li, R. M. Thorne, B. Ni, L. R. Lyons, V. Angelopoulos, Y. Ebihara, J. W. Bonnell, O. Le Contel, and U. Auster, Structures of dayside whistler-mode waves deduced from conjugate diffuse aurora, J. Geophys. Res. **118**, 664 (2013).

[17] B. Ni, R. M. Thorne, Y. Y. Shprits, and J. Bortnik, Resonant scattering of plasma sheet electrons by whistler-mode chorus: Contribution to diffuse auroral precipitation, Geophys. Res. Lett. **35**, 2008GL034032 (2008).

[18] B. Ni, R. M. Thorne, N. P. Meredith, R. B. Horne, and Y. Y. Shprits, Resonant scattering of plasma sheet electrons leading to diffuse auroral precipitation: 2. Evaluation for whistler mode chorus waves, J. Geophys. Res. **116**, A4 (2011).

[19] M. F. Ivarsen, J.-P. St-Maurice, Y. Jin, J. Park, W. Miloch, A. Spicher, Y.-S. Kwak, and L. B. N. Clausen, Steepening plasma density spectra in the ionosphere: The crucial role played by a strong E-region, J. Geophys. Res. **126**, e2021JA029401 (2021).

[20] R. A. Greenwald, Diffuse radar aurora and the gradient drift instability, J. Geophys. Res. **79**, 4807 (1974).

[21] M. F. Ivarsen, Y. Jin, A. Spicher, W. Miloch, and L. B. N. Clausen, The lifetimes of plasma structures at high latitudes, J. Geophys. Res. **126**, e2020JA028117 (2021).

[22] M. F. Ivarsen, J.-P. St-Maurice, Y. Jin, J. Park, L. M. Buschman, and L. B. Clausen, To what degree does the high-energy aurora destroy F-region irregularities? Front. Astron. Space Sci. **11**, 1309136 (2024).

[23] J. D. Sahr and B. G. Fejer, Auroral electrojet plasma irregularity theory and experiment: A critical review of present understanding and future directions, J. Geophys. Res. **101**, 26893 (1996).

[24] M. Wiltberger, V. Merkin, B. Zhang, F. Toffoletto, M. Oppenheim, W. Wang, J. G. Lyon, J. Liu, Y. Dimant, M. I. Sitnov, and G. K. Stephens, Effects of electrojet turbulence on a magnetosphere-ionosphere simulation of a geomagnetic storm, J. Geophys. Res. **122**, 5008 (2017).

[25] M. Oppenheim, N. Otani, and C. Ronchi, Saturation of the Farley-Buneman instability via nonlinear electron E×B drifts, J. Geophys. Res. **101**, 17273 (1996).

[26] D. L. Hysell, in *Auroral Dynamics and Space Weather*, edited by Y. Zhang and L. J. Paxton (American Geophysical Union, Washington, DC, 2015), Chap. 14, pp. 191–209.

[27] D. T. Farley, A plasma instability resulting in field-aligned irregularities in the ionosphere, J. Geophys. Res. **68**, 6083 (1963).

[28] O. Buneman, Excitation of field aligned sound waves by electron streams, Phys. Rev. Lett. **10**, 285 (1963).

[29] M. F. Ivarsen, Y. Miyashita, J.-P. St-Maurice, G. C. Hussey, B. Pitzel, D. Galeschuk, S. Marei, R. B. Horne, Y. Kasahara, S. Matsuda, S. Kasahara, K. Keika, Y. Miyoshi, K. Yamamoto, A. Shinbori, D. R. Huyghebaert, A. Matsuoka, S. Yokota, and F. Tsuchiya, Characteristic E-region plasma signature of magnetospheric wave-particle interactions, Phys. Rev. Lett. **134**, 145201 (2025).

[30] M. F. Ivarsen, J.-P. St-Maurice, G. C. Hussey, K. McWilliams, Y. Jin, D. R. Huyghebaert, Y. Miyashita, and D. Sibeck, preceding paper, Eastward transients in the dayside ionosphere. II. A parallel-plate capacitorlike effect, Phys. Rev. E **112**, 045203 (2025).

[31] D. Huyghebaert, G. Hussey, J. Vierinen, K. McWilliams, and J.-P. St-Maurice, ICEBEAR: An all-digital bistatic coded continuous-wave radar for studies of the E region of the ionosphere, Radio Sci. **54**, 349 (2019).

[32] A. Lozinsky, G. Hussey, K. McWilliams, D. Huyghebaert, and D. Galeschuk, ICEBEAR-3D: A low elevation imaging radar using a non-uniform coplanar receiver array for E region observations, Radio Sci. **57**, e2021RS007358 (2022).

[33] M. F. Ivarsen, A. Lozinsky, J.-P. St-Maurice, A. Spicher, D. Huyghebaert, G. C. Hussey, D. Galeschuk, B. Pitzel, and J. Vierinen, The distribution of small-scale irregularities in the E-region, and its tendency to match the spectrum of field-aligned current structures in the F-region, J. Geophys. Res. **128**, e2022JA031233 (2023).

[34] B. G. Fejer, The equatorial ionospheric electric fields. A review, J. Atmos. Terr. Phys. **43**, 377 (1981).

[35] M. F. Ivarsen, J.-P. St-Maurice, G. C. Hussey, D. R. Huyghebaert, and M. D. Gillies, Point-cloud clustering and tracking algorithm for radar interferometry, Phys. Rev. E **110**, 045207 (2024).

[36] M. F. Ivarsen, J.-P. St-Maurice, D. R. Huyghebaert, M. D. Gillies, F. Lind, B. Pitzel, and G. C. Hussey, Deriving the ionospheric electric field from the bulk motion of radar aurora in the E-region, J. Geophys. Res. **129**, e2024JA033060 (2024).

[37] N. E. Papitashvili and J. H. King, OMNI Hourly Data {Data Set], NASA Space Physics Data Facility (2020), https://doi.org/10.48322/1shr-ht18.

[38] J.-H. Li, X.-Z. Zhou, S. Wang, Z.-Y. Liu, Q.-G. Zong, S.-T. Yao, A. V. Artemyev, Y. Omura, L. Li, C. Yue, and Q.-Q. Shi, Bow shock ripples and their modulation of whistler wave packets: MMS observations, Geophys. Res. Lett. **51**, e2024GL111590 (2024).

[39] E. Krämer, F. Koller, J. Suni, A. T. LaMoury, A. Pöppelwerth, G. Glebe, T. Mohammed-Amin, S. Raptis, L. Vuorinen, S. Weiss, N. Xirogiannopoulou, M. Archer, X. Blanco-Cano, H. Gunell, H. Hietala, T. Karlsson, F. Plaschke, L. Preisser, O. Roberts, C. Simon Wedlund *et al.*, Jets downstream of collisionless shocks: Recent discoveries and challenges, Space Sci. Rev. **221**, 4 (2025).

[40] Y. Yang, L. Liu, W. Li, Y. Chen, H. Le, R. Zhang, and X. Zhao, Localized plasma density peak at middle latitudes during the April 2023 geomagnetic storm, J. Geophys. Res. **129**, e2023JA032165 (2024).

[41] R. Hajra, B. T. Tsurutani, Q. Lu, R. B. Horne, G. S. Lakhina, X. Yang, P. Henri, A. Du, X. Gao, R. Wang, and S. Lu, The April 2023 SYM-H = −233 nT geomagnetic storm: A classical event, arXiv:2409.08118.

[42] Z. Mošna, V. Barta, K. A. Berényi, J. Mielich, T. Verhulst, D. Kouba, J. Urbář, J. Chum, P. Koucka Knizova, H. Marew, K. Podolská, and R. Bojilova, March and April 2023 ionospheric storms in the period of the Solar Cycle 25, Front. Astron. Space Sci. **11**, 1462160 (2024).

[43] G. K. Davis, History of the NOAA satellite program, J. Appl. Remote Sens. **1**, 012504 (2007).

[44] D. S. Evans, Polar orbiting environmental satellite space environment monitor-2: Instrument description and archive data, NOAA Technical Memorandum OAR SEC-93 (2000), https://repository.library.noaa.gov/view/noaa/19636.

[45] M. F. Ivarsen, Y. Jin, A. Spicher, J.-P. St-Maurice, J. Park, and D. Billett, GNSS scintillations in the cusp, and the role of precipitating particle energy fluxes, J. Geophys. Res. **128**, e2023JA031849 (2023).

[46] Y. Jin, J. I. Moen, K. Oksavik, A. Spicher, L. B. N. Clausen, and W. J. Miloch, GPS scintillations associated with cusp dynamics and polar cap patches, J. Space Weather Space Clim. **7**, A23 (2017).

[47] Y. Miyoshi, I. Shinohara, T. Takashima, K. Asamura, N. Higashio, T. Mitani, S. Kasahara, S. Yokota, Y. Kazama, S.-Y. Wang, S. W. Y. Tam, P. T. P. Ho, Y. Kasahara, Y. Kasaba, S. Yagitani, A. Matsuoka, H. Kojima, Y. Katoh, K. Shiokawa, and K. Seki, Geospace exploration project ERG, Earth Planets Space **70**, 101 (2018).

[48] S. Kasahara, S. Yokota, T. Mitani, K. Asamura, M. Hirahara, Y. Shibano, and T. Takashima, Medium-energy particle experiments—electron analyzer (MEP-e) for the exploration of energization and radiation in geospace (ERG) mission, Earth Planets Space **70**, 69 (2018).

[49] M. Fukizawa, T. Sakanoi, Y. Miyoshi, K. Hosokawa, K. Shiokawa, Y. Katoh, Y. Kazama, A. Kumamoto, F. Tsuchiya, Y. Miyashita, Y. M. Tanaka, Y. Kasahara, M. Ozaki, A. Matsuoka, S. Matsuda, M. Hikishima, S. Oyama, Y. Ogawa, S. Kurita, and R. Fujii, Electrostatic electron cyclotron harmonic waves as a candidate to cause pulsating auroras, Geophys. Res. Lett. **45**, 12,661 (2018).

[50] P. Alken, E. Thébault, C. D. Beggan, H. Amit, J. Aubert, J. Baerenzung, T. N. Bondar, W. J. Brown, S. Califf, A. Chambodut, A. Chulliat, G. A. Cox, C. C. Finlay, A. Fournier, N. Gillet, A. Grayver, M. D. Hammer, M. Holschneider, L. Huder, G. Hulot *et al.*, International geomagnetic reference field: The thirteenth generation, Earth Planets Space **73**, 49 (2021).

[51] Y. Kasahara, Y. Kasaba, H. Kojima, S. Yagitani, K. Ishisaka, A. Kumamoto, F. Tsuchiya, M. Ozaki, S. Matsuda, T. Imachi, Y. Miyoshi, M. Hikishima, Y. Katoh, M. Ota, M. Shoji, A. Matsuoka, and I. Shinohara, The plasma wave experiment (PWE) on board the arase (ERG) satellite, Earth Planets Space **70**, 86 (2018).

[52] A. Kumamoto, F. Tsuchiya, Y. Kasahara, Y. Kasaba, H. Kojima, S. Yagitani, K. Ishisaka, T. Imachi, M. Ozaki, S. Matsuda, M. Shoji, A. Matsuoka, Y. Katoh, Y. Miyoshi, and T. Obara, High Frequency Analyzer (HFA) of Plasma Wave Experiment (PWE) onboard the Arase spacecraft, Earth Planets Space **70**, 82 (2018).

[53] Z.-K. Xie, Q. G. Zong, J. Ren, C. Yue, Z.-Y. Liu, J.-J. Liu, Z.-J. Hu, X.-Y. Li, Z.-F. Yin, Y. Yan, L. Li, and J. W. Gjerloev, Global ULF waves excited by solar wind dynamic pressure impulses: 1. Timescales and geomagnetic activity dependence, J. Geophys. Res. **128**, e2023JA031813 (2023).

[54] X.-Y. Li, Q.-G. Zong, J.-J. Liu, Z.-F. Yin, Z.-J. Hu, X.-Z. Zhou, C. Yue, Z.-Y. Liu, X.-X. Zhao, Z.-K. Xie, J. B. Blake, C. T. Russell, R. E. Ergun, and P.-A. Lindqvist, Comparative study of dayside pulsating auroras induced by ultralow-frequency waves, Universe **9**, 258 (2023).

[55] K. Hosokawa, A. Kadokura, N. Sato, S. E. Milan, M. Lester, G. Bjornsson, and T. Saemundsson, Electric field modulation behind pulsating aurora, J. Geophys. Res. **113**, (2008).

[56] K. Hosokawa, T. Tsugawa, K. Shiokawa, Y. Otsuka, N. Nishitani, T. Ogawa, and M. R. Hairston, Dynamic temporal evolution of polar cap tongue of ionization during magnetic storm, J. Geophys. Res. **115**, A12333 (2010).

[57] Y. Nishimura, M. R. Lessard, Y. Katoh, Y. Miyoshi, E. Grono, N. Partamies, N. Sivadas, K. Hosokawa, M. Fukizawa, M. Samara, R. G. Michell, R. Kataoka, T. Sakanoi, D. K. Whiter, S.-i. Oyama, Y. Ogawa, and S. Kurita, Diffuse and pulsating aurora, Space Sci. Rev. **216**, 4 (2020).

[58] K. Hosokawa, Y. Miyoshi, M. Ozaki, S.-I. Oyama, Y. Ogawa, S. Kurita, Y. Kasahara, Y. Kasaba, S. Yagitani, S. Matsuda, F. Tsuchiya, A. Kumamoto, R. Kataoka, K. Shiokawa, T. Raita, E. Turunen, T. Takashima, I. Shinohara, and R. Fujii, Multiple time-scale beats in aurora: Precise orchestration via magnetospheric chorus waves, Sci. Rep. **10**, 3380 (2020).

[59] R. Chen, Y. Miyoshi, X. Gao, Q. Lu, B. T. Tsurutani, K. Hosokawa, T. Hori, Y. Ogawa, S.-I. Oyama, Y. Kasahara, S. Matsuda, S. Nakamura, A. Matsuoka, and I. Shinohara, Observational evidence for three time-scale modulations in the pulsating aurora, Geophys. Res. Lett. **51**, e2024GL108253 (2024).

[60] R. J. Redmon, W. F. Denig, L. M. Kilcommons, and D. J. Knipp, New DMSP database of precipitating auroral electrons and ions, J. Geophys. Res. **122**, 9056 (2017).

[61] X. Fang, C. E. Randall, D. Lummerzheim, W. Wang, G. Lu, S. C. Solomon, and R. A. Frahm, Parameterization of monoenergetic electron impact ionization, Geophys. Res. Lett. **37**, 2010GL045406 (2010).

[62] P. T. Jayachandran, R. B. Langley, J. W. MacDougall, S. C. Mushini, D. Pokhotelov, A. M. Hamza, I. R. Mann, D. K. Milling, Z. C. Kale, R. Chadwick, T. Kelly, D. W. Danskin, and C. S. Carrano, Canadian high arctic ionospheric network (CHAIN), Radio Sci. **44**, 2008RS004046 (2009).

[63] See Supplemental Material at http://link.aps.org/supplemental/10.1103/r6bv-pzlq for details.

[64] G. Blinstrubas, A. English, D. J. Stuart, D. L. Hampton, L. Lamarche, Y. Nishimura, and S. Datta-Barua, Comparative hypothesis testing of auroral ionospheric layer causing global navigation satellite system scintillation, Space Weather **23**, e2024SW004069 (2025).

[65] C. N. Mitchell, L. Alfonsi, G. De Franceschi, M. Lester, V. Romano, and A. W. Wernik, GPS TEC and scintillation measurements from the polar ionosphere during the October 2003 storm, Geophys. Res. Lett. **32**, L12S03 (2005).

[66] P. M. Kintner, B. M. Ledvina, and E. R. de Paula, GPS and ionospheric scintillations, Space Weather **5**, 2006SW000260 (2007).

[67] R. Burston, I. Astin, C. Mitchell, L. Alfonsi, T. Pedersen, and S. Skone, Correlation between scintillation indices and gradient drift wave amplitudes in the northern polar ionosphere, J. Geophys. Res. **114**, 2009JA014151 (2009).

[68] M. F. Ivarsen, J.-P. St-Maurice, G. C. Hussey, D. Galeschuk, A. Lozinsky, B. Pitzel, and K. A. McWilliams, An algorithm to separate ionospheric turbulence radar echoes from those of meteor trails in large data sets, J. Geophys. Res. **128**, e2022JA031050 (2023).

[69] M. F. Ivarsen, M. D. Gillies, D. R. Huyghebaert, J.-P. St-Maurice, A. Lozinsky, D. Galeschuk, E. Donovan, and G. C. Hussey, Turbulence embedded into the ionosphere by electromagnetic waves, J. Geophys. Res. **129**, e2023JA032310 (2024).

[70] A. Belehaki and G. Rostoker, Relationship between the dayside auroral electrojets and the DPY current, J. Geophys. Res. **101**, 2397 (1996).

[71] W. Lyatsky and D. Sibeck, Central plasma sheet disruption and the formation of dayside poleward moving auroral events, J. Geophys. Res. **102**, 17625 (1997).

[72] Y. Miyoshi, T. Hori, M. Shoji, M. Teramoto, T. F. Chang, T. Segawa, N. Umemura, S. Matsuda, S. Kurita, K. Keika, Y. Miyashita, K. Seki, Y. Tanaka, N. Nishitani, S. Kasahara, S. Yokota, A. Matsuoka, Y. Kasahara, K. Asamura, T. Takashima *et al.*, The ERG science center, Earth Planets Space **70**, 96 (2018).

[73] https://ergsc.isee.nagoya-u.ac.jp/data_info/erg.shtml.en.

[74] A. Matsuoka, M. Teramoto, R. Nomura, M. Nosé, A. Fujimoto, Y. Tanaka, M. Shinohara, T. Nagatsuma, K. Shiokawa, Y. Obana, Y. Miyoshi, M. Mita, T. Takashima, and I. Shinohara, The ARASE (ERG) magnetic field investigation, Earth Planets Space **70**, 43 (2018).

[75] ICEBEAR data policy, University of Saskatchewan, Saskatoon, Canada, http://icebear.usask.ca/icebeardata.php?page=1.

[76] SuperMAG, U.S. National Science Foundation, Alexandria, https://supermag.jhuapl.edu/mag/.

[77] OMNIWeb Plus, NASA, Washington, DC, https://omniweb.gsfc.nasa.gov/.

[78] E. G. Thomas and S. G. Shepherd, Statistical patterns of ionospheric convection derived from mid-latitude, high-latitude, and polar superdarn HF radar observations, J. Geophys. Res. **123**, 3196 (2018).

[79] SuperDARNCanada/globus, GitHub, San Francisco, https://github.com/SuperDARNCanada/globus.

[80] NOAA, Washington, DC, https://www.ngdc.noaa.gov/stp/satellite/poes/.